Sacrificial Species Approach to Designing Robust Transition Metal Phosphide Cathodes for Alkaline Water Electrolysis in Discontinuous Operation

Ik-Sun Kim,[ab] Hyun-Seok Cho*[a], MinJoong Kim,*[a] Hyun-Jung Oh,[c] Sang-Yeon Lee,[c] Yong-Kul Lee,[c] Changsoo Lee, [a] Jae Hun Lee,[a] Won Chul Cho,[a] Sang-Kyung Kim, [a] Jong Hoon Joo, [bd] and Chang-Hee Kim*[a]

a. Hydrogen Research Department, Korea Institute of Energy Research, Daejeon, 34129, Republic of Korea
b. Department of Urban, Energy, and Environmental Engineering, Chungbuk National University, Cheongju, 28644, Republic of Korea
c. Department of Chemical Engineering, Dankook University, Yongin, 16890, Republic of Korea
d. Department of Advanced Material Engineering, Chungbuk National University, Cheongju, 28644, Republic of Korea

Supporting Information

Experimental

1. Sample Preparation

Before electrodeposition, the Ni substrate (ATI 201™, 99.6 % purity, ATI Metals Corp., US) was electrochemically degreased in 25 wt.% NaOH at 85 °C for 2 min, rinsed with deionized water, treated with 20 % HCl at room temperature for 2 min to remove the surface oxides, and rinsed with deionized water again. Coatings of cobalt phosphide (CoP_x) and manganese-cobalt phosphide ($Mn_nCo_{1-n}P_x$) were deposited on Ni substrate and then embedded in a polyether ether ketone holder, leaving an open area of 1.77 cm^2. The two-electrode system was configured with Ni plate as the counter electrode, the distance between the working and counter electrodes was 2 cm, and the temperature was 25 ℃. The compositions of electrodeposition baths are listed in **Table S11**. The depositions of both CoP_x and $Mn_nCo_{1-n}P_x$ were performed at a constant current density of -112 mA cm^{-2} for 450 s. During deposition, hydrogen bubbles were vigorously produced at the electrode surface.

2. Electrochemical Analysis

The typical three-electrode measurement was performed in 1 M KOH solution at 25 ℃, using CoP_x/ $Mn_nCo_{1-n}P_x$ as the working electrode with an open area of 0.785 cm^2, Pt plate (i.e., 50 mm x 50 mm) and a graphite rod (i.e., outer diameter 6 mm, length 145 mm) with a glass frit as the counter electrode, and Hg/HgO as the reference. The electrochemical control and data acquisition employed SP-240 (Biologic) with EC-lab software. The EIS measurement was made in the frequency range from 100 kHz to 10 mHz at -1.1 V (vs. Hg/HgO) with a sinusoidal

amplitude of 10 mV. LSV was used to evaluate the HER activity in the range from -0.9 to -1.6 V (vs. Hg/HgO) with a scan rate of 1 mV s^{-1}. The electrical circuit was left open during the shut-down condition, no current or voltage was applied, and the potential changes were recorded against the reference electrode. The LSV experiment was also carried out after the shut-down condition to compare the HER activity with the pristine curve. The LSV curves were IR-compensated based on the high frequency resistance acquired from EIS measurement. Since HER activity of non-precious metals in aqueous solution were reported the possible overestimation due to the re-deposition of Pt clusters from the counter electrode onto the non-precious metal working electrode, the aqueous HER data with Pt counter electrode may produce inaccuracies for HER activity measurement. In this study, the HER activities of $CoP_x/Mn_nCo_{1-n}P_x$ with a carbon rod counter electrode were compared and showed no deviation regardless of counter electrodes, as shown in **Fig. S16**. The potential for HER activity of the CoP_x and $Mn_nCo_{1-n}P_x$ was converted to RHE scales. To convert $E_{Hg/HgO}$ to E_{RHE}, following equation was used: $E_{RHE} = E_{Hg/HgO} + 0.097 + 0.059pH$.

3. Structure and Surface Characterizations

The surface morphologies and chemical composition were analyzed by Scanning Electron Microscope (SEM, HITACHI, S-4800) coupled with Energy Dispersive X-ray Spectroscopy (EDS, HORIBA, X-Max50). Before SEM analysis, all samples were coated with Os. In addition, Transmission Electron Microscopy (TEM, FEI, Talos F200X) and TEM-EDS (Bruker, Super X EDS system) analysis were carried out to investigate details of surface crystalline of $Mn_nCo_{1-n}P_x$. To prepare cross-sectional TEM sample, ion cutting using Focused Ion Beam (FIB, FEI, Helios G4) was implemented. The samples were coated with carbon

followed by Pt before FIB cutting. XRD patterns for bulk and thin surface layer were recorded with the X-Ray diffractometer (Rig aku, SmartLab) and the low-angle XRD X-ray diffractometer (low-angle XRD, Rigaku, D/MAX-2500), respectively. The stainless steel 316 was used as a substrate for low-angle XRD (CoP_x/SUS and $Mn_nCo_{1-n}P_x$/SUS) because the identifications were disturbed by strong Ni peaks on the Ni substrates (**Fig. S17**.). The oxidation state and electronic state of Co, Mn, and O were investigated by an XPS spectrometer (Thermo VG Scientific, K-Alpha).

4. X-ray Absorption Measurements

XAS spectra at the Co K-edge (7.708 keV) were collected at Beamline 8C of the Pohang Light Source (PLS), which has a flux of 2×10^{12} photons s^{-1} at 300 mA and 3.0 GeV. The samples were electroplated on Ni foam for measurement in the transmission mode. For the *in situ* XAS, a home-made electrochemical cell with a 5 mm gap was used for transmission measurement. The cell used N_2-purged 1.0 M KOH as the electrolyte solution, with a Pt wire counter electrode and a Hg/HgO reference electrode. The XAFS data were analyzed using Winxas 3.1 software.

Table S1. A comparison with reported HER activity on CoP_x in alkaline electrolyte.

Catalyst	Overpotential@ 10 mA cm^{-2}	ref
CoP_x/Ni	**65 mV**	**This work**
Ni substrate	201 mV	This work
Mn-Co-P/Ti	76 mV	1
$Zn_{0.08}Co_{0.92}P$/TM	67 mV	2
CoP/CC	209 mV	3
Co_2P/RGO	88 mV	4
CoP-MNA	54 mV	5
np-CoP NWs/Ti	100 mV	6
CoP NS/C	111 mV	7
CoP nanoarrays/CC	95 mV	8
CoP_3 NAs/CFP	119 mV	9

Table S2. Possible redox couples of Co in alkaline electrolyte.[10]

Redox couple	Reaction	Potential [$V_{Hg/HgO}$]
$Co/Co(OH)_2$	$Co + 2OH^- \rightarrow Co(OH)_2 + 2e^-$	-0.818
Co/CoO	$Co + 2OH^- \rightarrow CoO + H_2O + 2e^-$	-0.792
Co/Co_3O_4	$3Co + 8OH^- \rightarrow Co_3O_4 + 4H_2O + 8e^-$	-0.661
Co/CoOOH	$2Co + 3OH^- \rightarrow CoOOH + H_2O + 3e^-$	-0.563
CoO/Co_3O_4	$3CoO + 2OH^- \rightarrow Co_3O_4 + H_2O + 2e^-$	-0.369
Co/CoO_2	$Co + 4OH^- \rightarrow CoO_2 + 2H_2O + 4e^-$	-0.282
$Co(OH)_2/Co_3O_4$	$3Co(OH)_2 + 2OH^- \rightarrow Co_3O_4 + 4H_2O + 2e^-$	-0.192
CoO/CoOOH	$CoO + OH^- \rightarrow CoOOH + H_2O + e^-$	-0.172
$Co(OH)_2$/CoOOH	$Co(OH)_2 + OH^- \rightarrow CoOOH + H_2O + e^-$	-0.054

Table S3. Kinetic parameters used for the construction of Evans diagram.

Possible reaction	Potential [V vs. Hg/HgO]	Kinetic parameter		
		i_0	α	b
$Co + 2OH^- \rightarrow Co(OH)_2 + 2e^-$	-0.827	5.0×10^{-5}	1.8	3.28×10^{-2}
$O_2 + 2H_2O + 4e^- \rightarrow 4OH^-$	0.304	2.5×10^{-42}	2.0	-2.95×10^{-2}

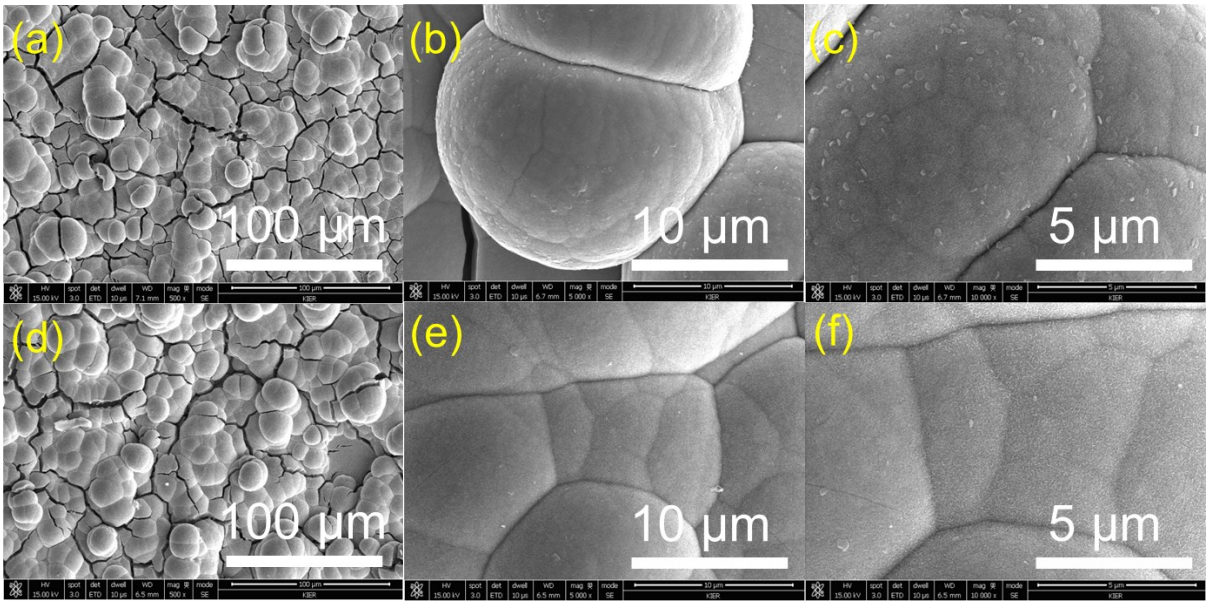

Fig. S1. (a),(b),(c) 500x, 5,000x, 10,000x of SEM images of the CoP_x. (d),(e),(f) 500x, 5,000x, 10,000x of SEM images of the CoP_x after shut-down for 5 h in 1M KOH.

Table S4. EDS result of CoP_x.

Element	Weight %	Atomic %
P	3.49	6.44
Co	96.51	93.56
Totals	100.00	100.00

Table S5. EDS result of CoP_x after hold off condition for 5 h in 1M KOH.

Element	Weight %	Atomic %
P	2.95	5.46
Co	97.05	94.54
Totals	100.00	100.00

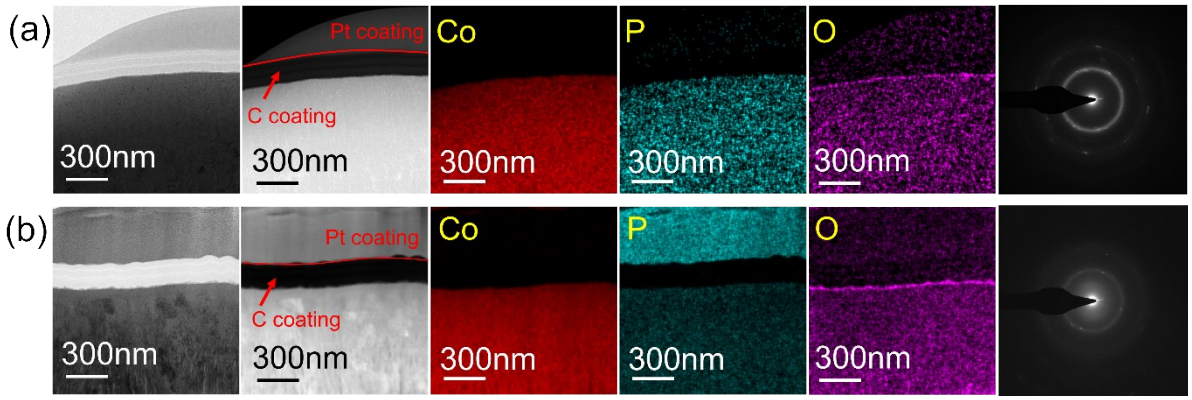

Fig. S2. (From left) TEM, STEM, TEM-EDS images and SAED pattern for CoP_x. (a) before hold-off condition (b) after hold-off for 5 h.

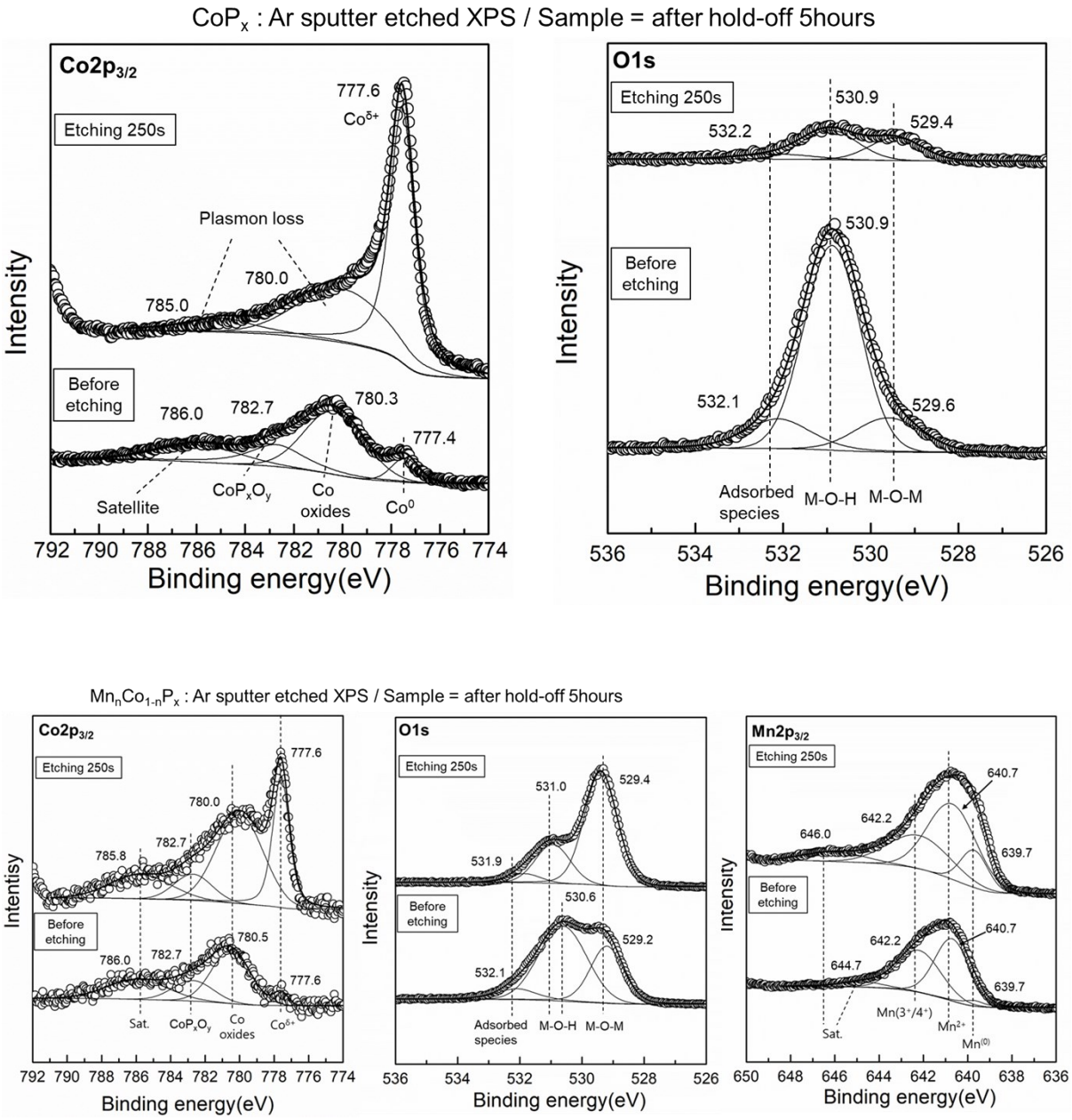

Fig. S3. The XPS depth profiles with Ar^+ ion sputter on electrodeposited CoP_x and $Mn_nCo_{1-n}P_x$

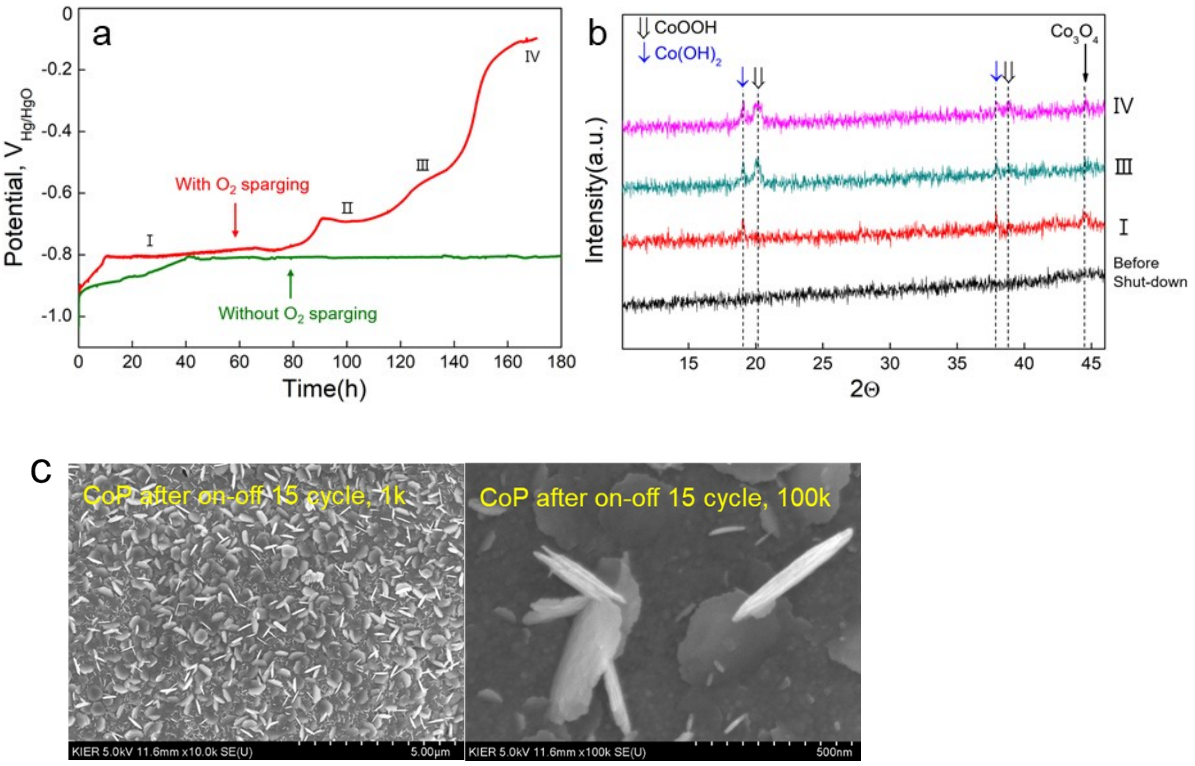

Below reactions are listed in **Table S2**.

$Co + 2OH^- \rightarrow Co(OH)_2 + 2e^-$: -0.818 V(Hg/HgO)

$Co + 2OH^- \rightarrow CoO + H_2O + 2e^-$: -0.792 V(Hg/HgO)

$3Co + 8OH^- \rightarrow Co_3O_4 + 4H_2O + 8e^-$: -0.661 V(Hg/HgO)

$2Co + 3OH^- \rightarrow CoOOH + H_2O + 3e^-$: -0.563 V(Hg/HgO)

$Co + 4OH^- \rightarrow CoO_2 + 2H_2O + 4e^-$: -0.282 V(Hg/HgO)

$3Co(OH)_2 + 2OH^- \rightarrow Co_3O_4 + 4H_2O + 2e^-$: -0.192 V(Hg/HgO)

$3CoO + 2OH^- \rightarrow Co_3O_4 + H_2O + 2e^-$: -0.369 V(Hg/HgO)

$Co(OH)_2 + OH^- \rightarrow CoOOH + H_2O + e^-$: -0.054 V(Hg/HgO)

$CoO + OH^- \rightarrow CoOOH + H_2O + e^-$: -0.172 V(Hg/HgO)

Fig. S4. (a) OCV change with sparging O_2 (b) XRD peaks of the samples with the different OCV range.[11-14] (c) surface of CoP_x after 15 on/off cycles

Table S6. Possible sacrificial anode and oxidation reaction.

Sacrificial species	Oxidation reaction	Potential [$V_{Hg/HgO}$]
Al	$Al + 3OH^- \rightarrow Al(OH)_3 + 3e^-$	-2.407
Cr	$Cr + 3OH^- \rightarrow Al(OH)_3 + 3e^-$	-1.577
Mn	$Mn + 2OH^- \rightarrow Mn(OH)_2 + 2e^-$	-1.657
Zn	$Zn + 2OH^- \rightarrow Zn(OH)_2 + 2e^-$	-1.346

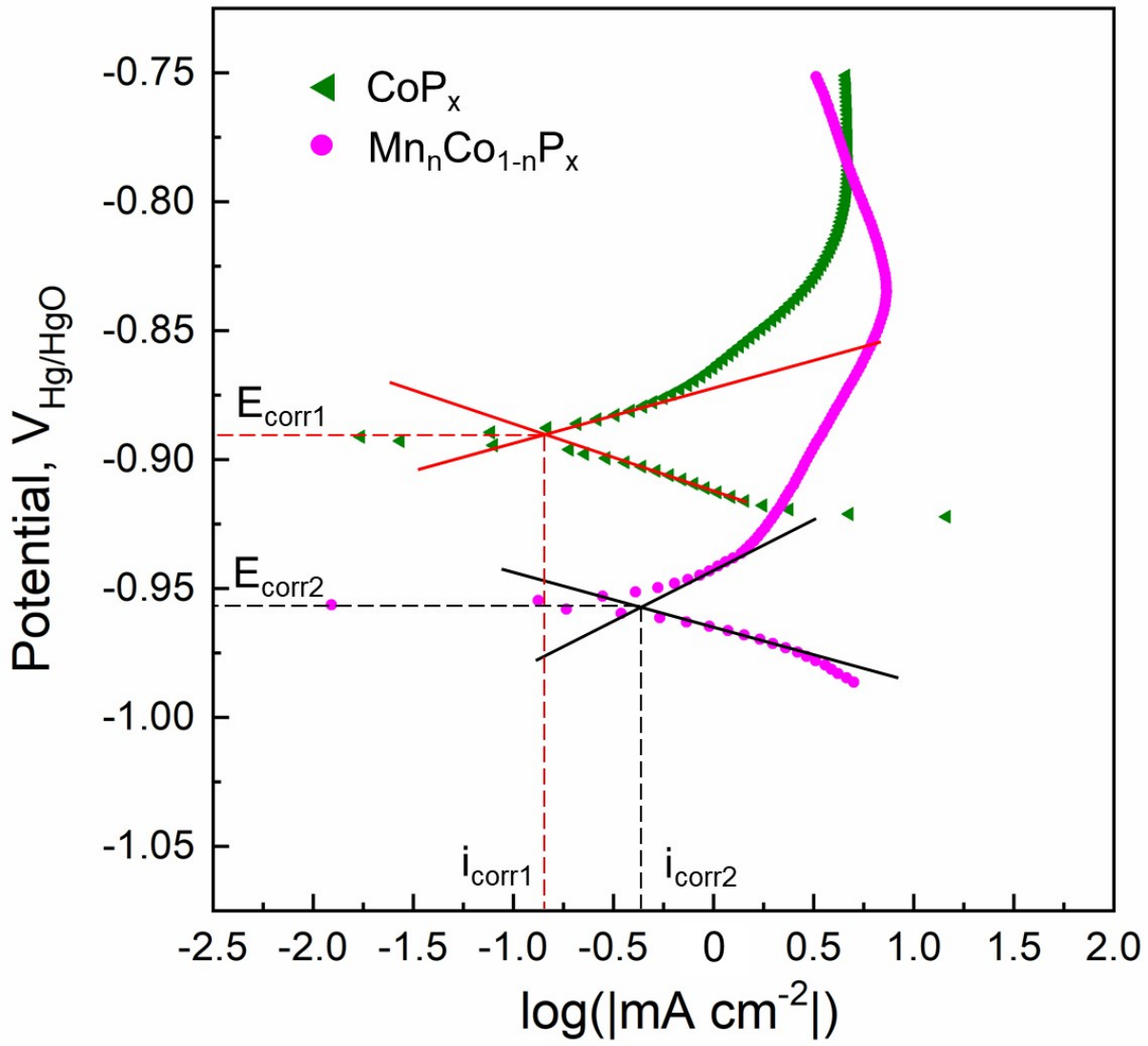

Fig. S5. Experimental cathodic and anodic polarization curve for CoP_x and $Mn_nCo_{1-n}P_x$ in 1 M KOH without O_2 sparging

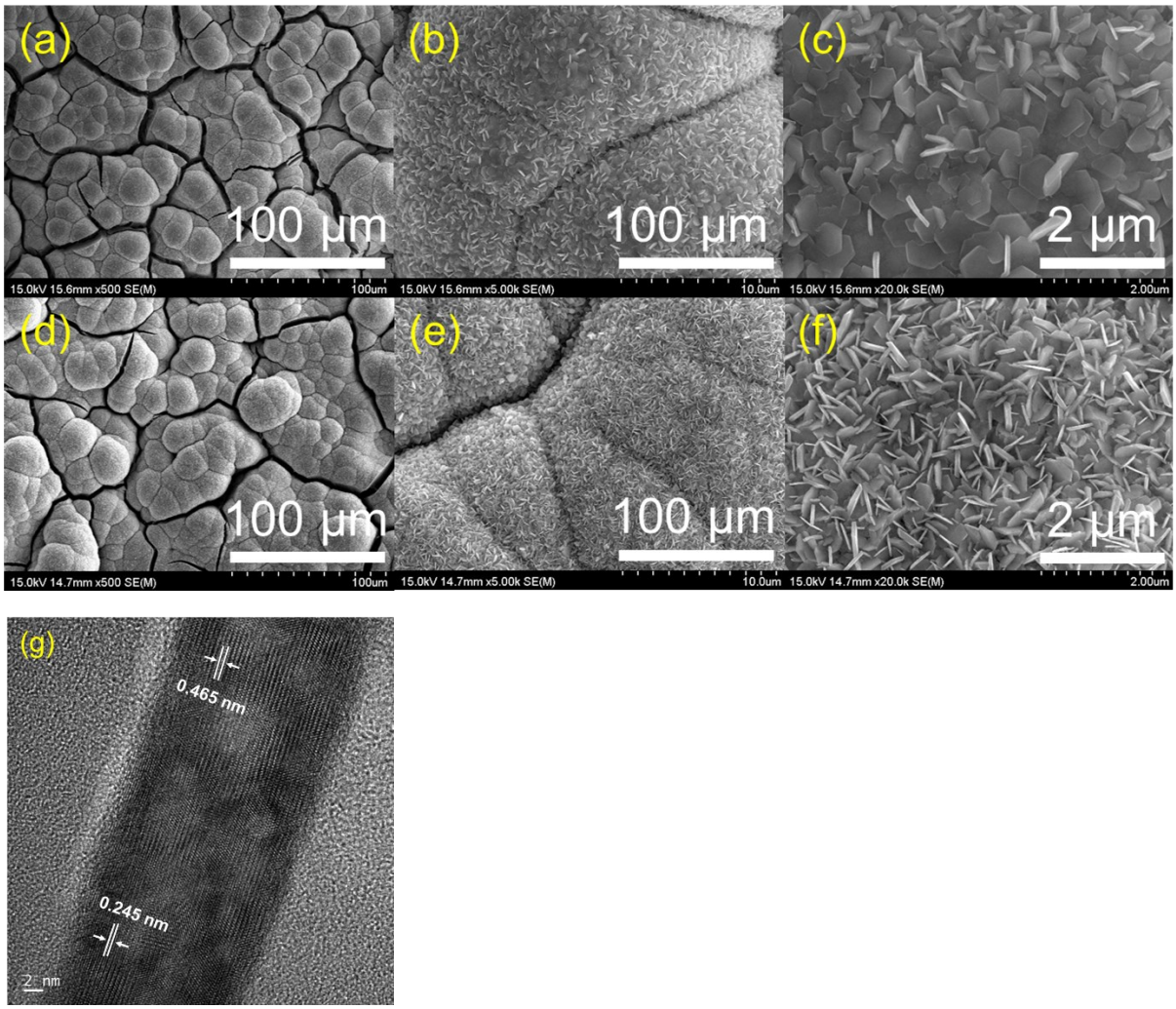

Fig. S6. (a),(b),(c) 500x, 5,000x, 10,000x of SEM images of the $Mn_nCo_{1-n}P_x$. (d),(e),(f) 500x, 5,000x, 10,000x of SEM images, (g) HRTEM images of the flake of the $Mn_nCo_{1-n}P_x$ before OCV condition in 1M KOH.

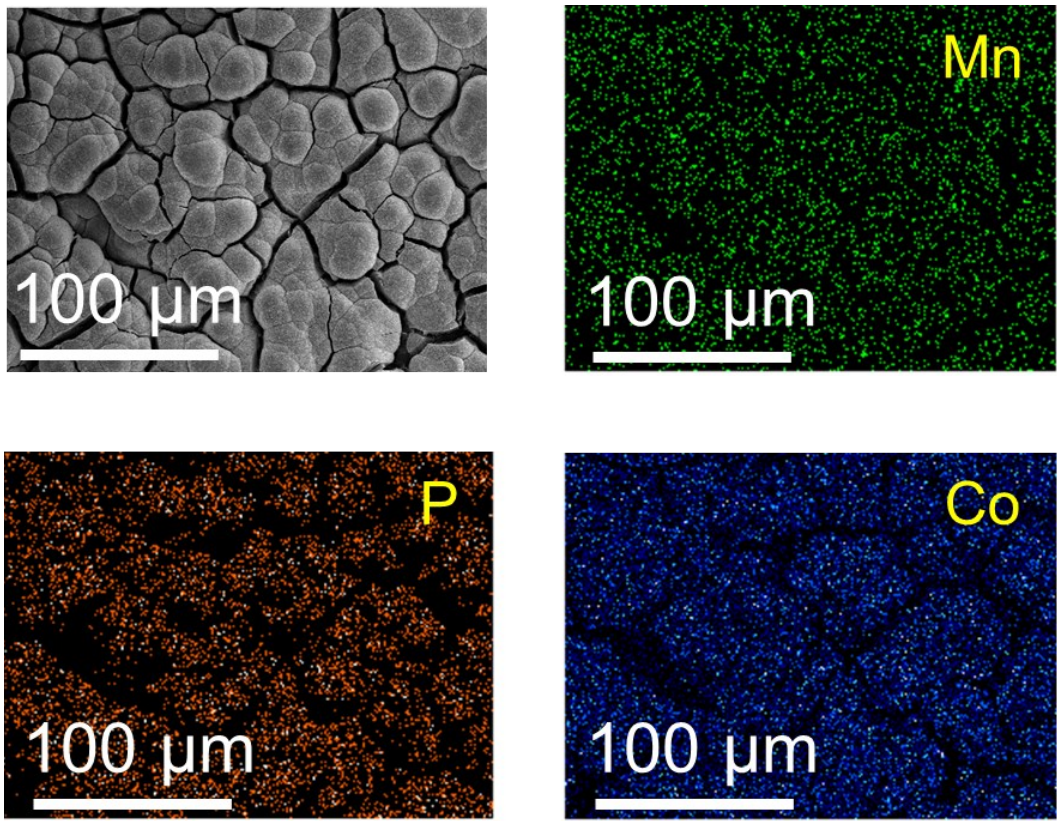

Fig. S7. EDS mapping of the $Mn_nCo_{1-n}P_x$ after HER.

Table S7. EDS result of $Mn_nCo_{1-n}P_x$ after HER.

Element	Weight %	Atomic %
P K	4.91	8.91
Mn K	4.94	5.05
Co K	90.16	86.04
Totals	100.00	100.00

Table S8. EDS result of $Mn_nCo_{1-n}P_x$ after OCV condition for 5 h in 1M KOH.

Element	Weight %	Atomic %
P K	4.77	8.65
Mn K	8.52	8.71
Co K	86.71	82.64
Totals	100.00	100.00

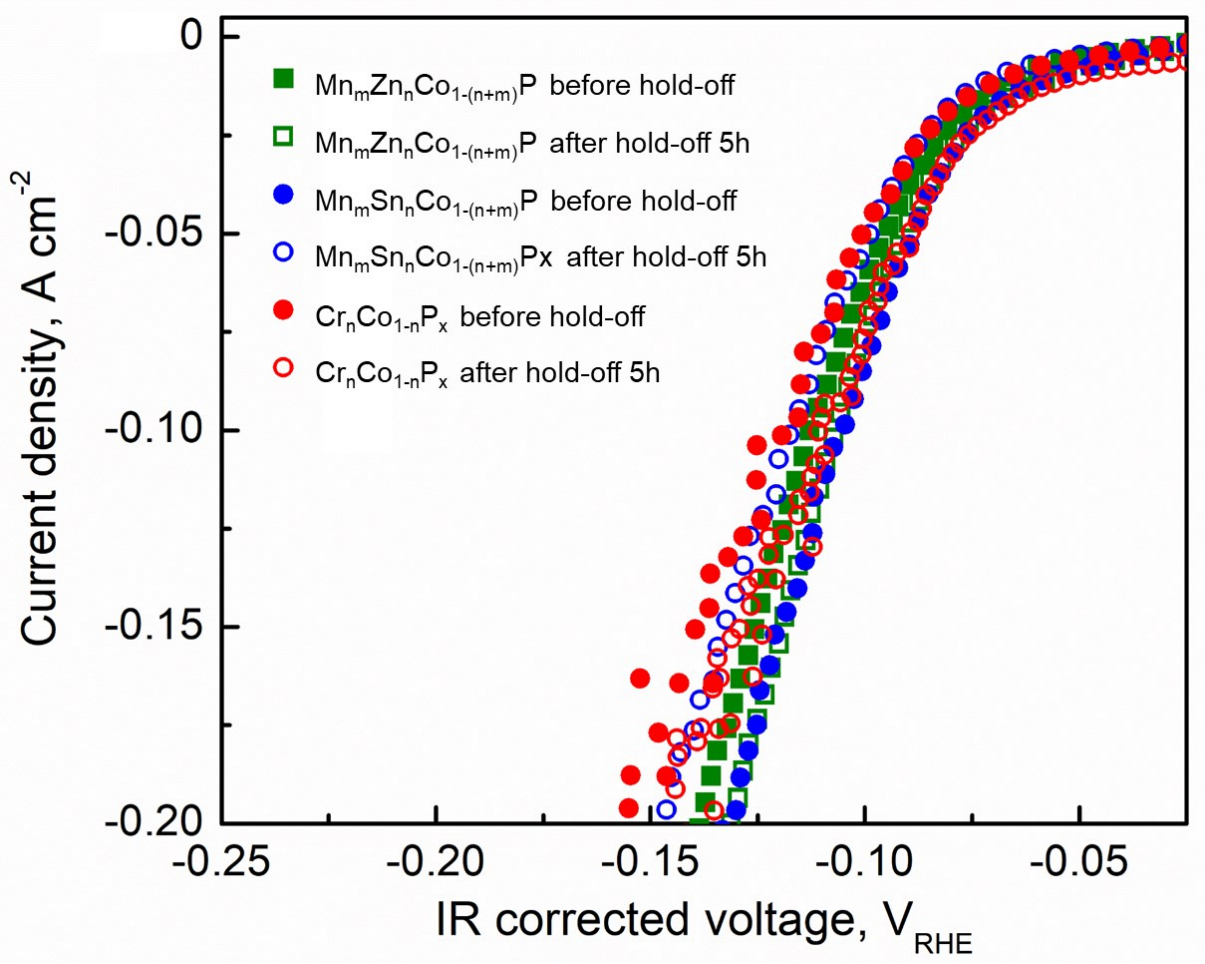

Fig. S8. The HER activity before and after hold-off for 5 hours of the CoPx-based various transition metal doped HER electrode.

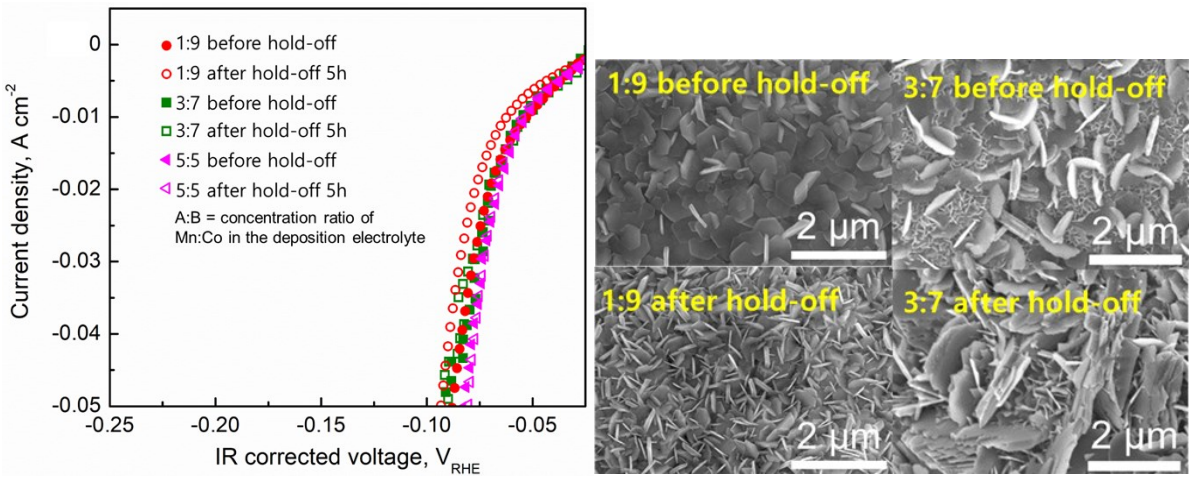

Fig. S9. The influence of Mn content on the structure, activity, and stability of the resulting $Mn_nCo_{1-n}P_x$ in both continuous and discontinuous operation

Table. S9 The chemical ratio of Mn and P for $Mn_nCo_{1-n}P_x$ as increasing of Mn contents

	before hold-off				after hold-off			
elements	Mn:Co=1:9		Mn:Co=3:7		Mn:Co=1:9		Mn:Co=3:7	
	weight %	Atomic %	weight %	Atomic %	Weight %	Atomic %	weight %	Atomic%
P	4.91	8.91	8.34	14.67	4.77	8.65	3.00	5.50
Mn	4.94	5.05	7.70	7.65	8.52	8.71	18.68	19.25
Co	90.16	86.04	83.96	77.68	86.71	82.64	78.32	75.25

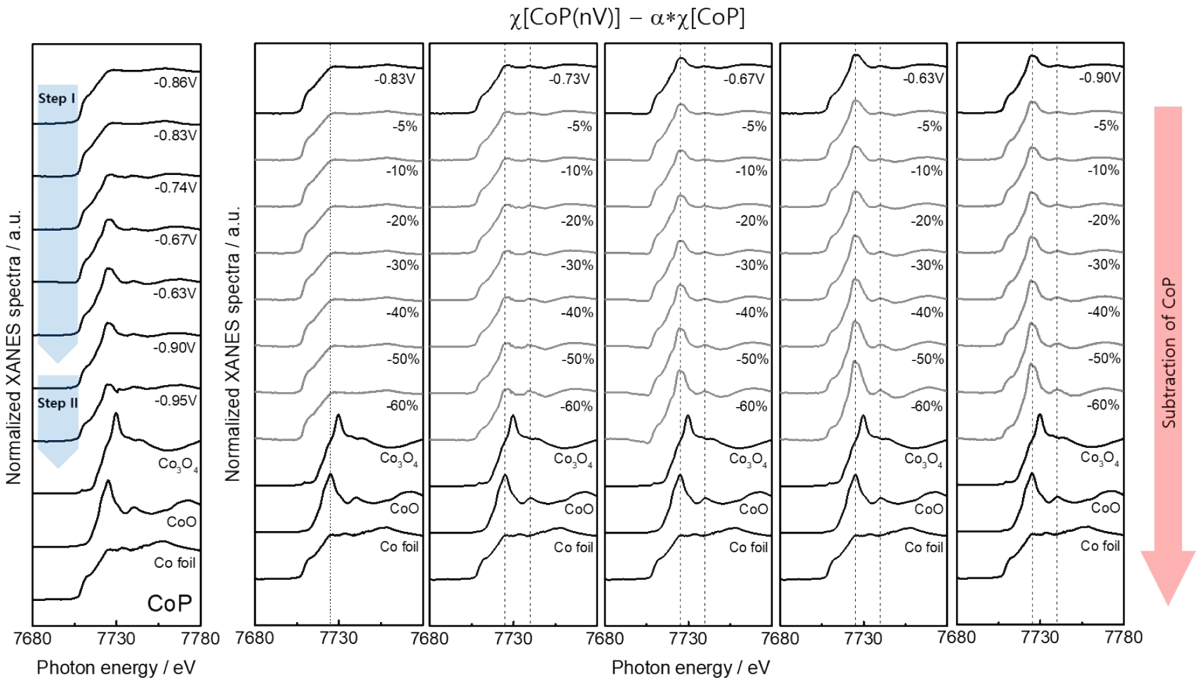

Fig. S10. Subtraction of the XANES spectrum of CoP_x from those obtained in CV cycles

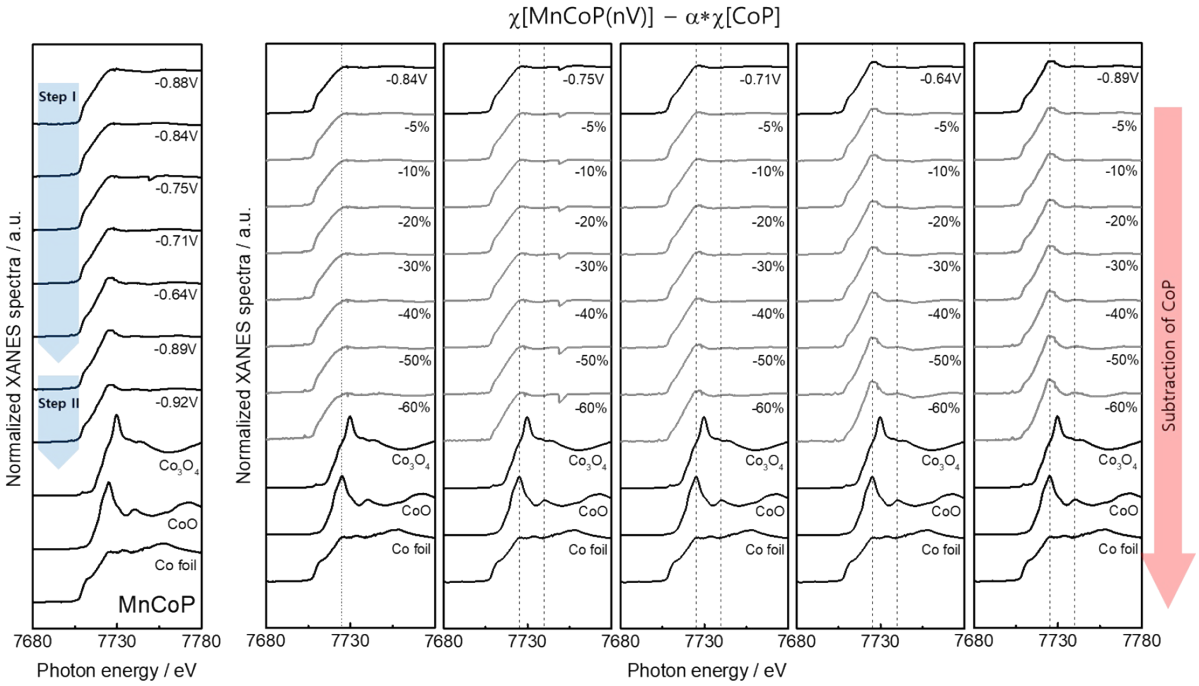

Fig. S11. Subtraction of the XANES spectrum of CoP_x from $Mn_nCo_{1-n}P_x$ those obtained in CV cycles

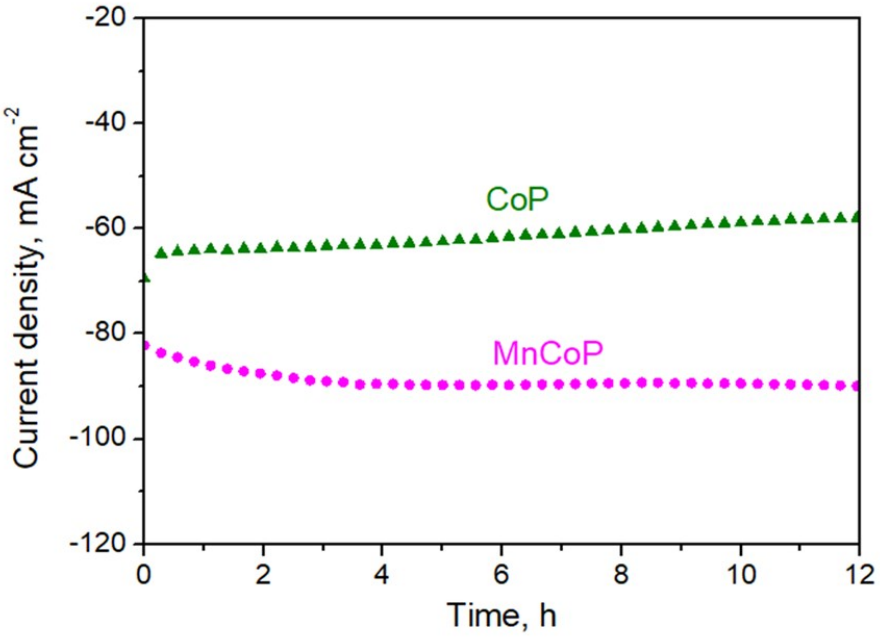

Fig. S12. The durability test of CoP_x and $Mn_nCo_{1-n}P_x$ electrodes in continuous operation (constant potential of -1.1 V (vs. Hg/HgO) in 1 M KOH at 25°C

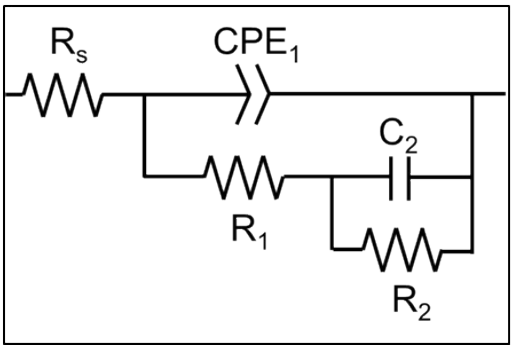

Fig. S13. 2TP equivalent circuit model for EIS fitting.

Table S10. Impedance parameters for equivalent circuit of the 2TP model obtained by fitting EIS experimental.

Parameter [units]	CoP_x			$Mn_nCo_{1-n}P_x$		
	Before on-off	After 15 cycles	After 50 cycles	Before on-off	After 15 cycles	After 50 cycles
RS [Ohm]	1.24	0.961	1.27	1.171	0.907	1.165
R1 [Ohm]	0.26	0.844	1.622	0.156	0.3	0.818
R2 [Ohm]	0.12	0.423	4.827	0.197	0.263	0.555
Q1 [F·s^(a-1)]	0.168	0.052	0.0016	0.367	0.082	96
a	0.890	0.963	1	0.76	1	0.967
CCPE [F]	0.1114	0.045	0.0016	0.143	0.082	0.0864
C_2 [F]	1.348	0.017	0.004	0.933	0.04	0.016

(i) Q_1 and a_1 are the constant and exponent, respectively, R_s is the solution resistance. R_1 represents th e HER charge transfer resistance, and R_2 is the resistance related to hydrogen adsorption.

CoPx after on-off 15 cycle

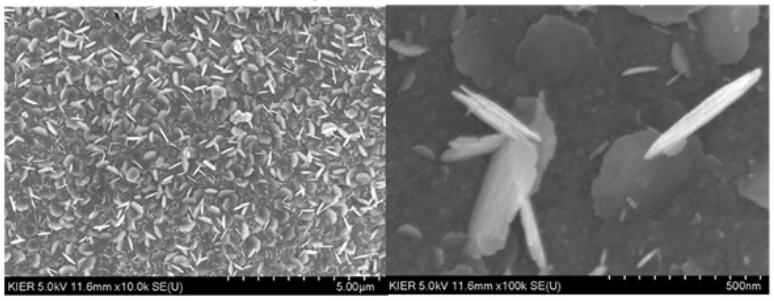

Element	Weight %	Atomic %
P K	2.03	3.79
Co K	97.97	96.21
Totals	100	100

$Mn_nCo_{1-n}P_x$ after on-off 15 cycle

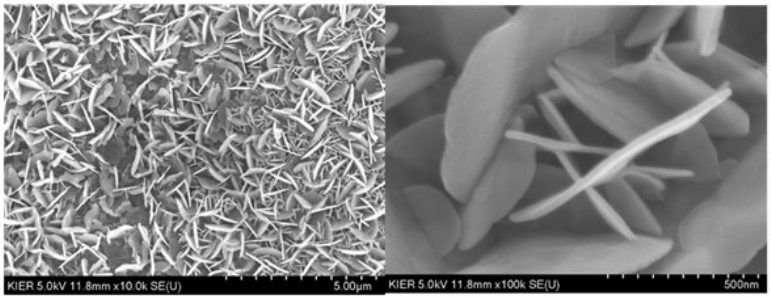

Element	Weight %	Atomic %
P K	2.62	4.83
Mn K	9.13	9.50
Co K	88.25	85.67
Totals	100	100

Fig. S14. SEM-EDS resuls for CoP_x and $Mn_nCo_{1-n}P_x$ in discontinuous operation

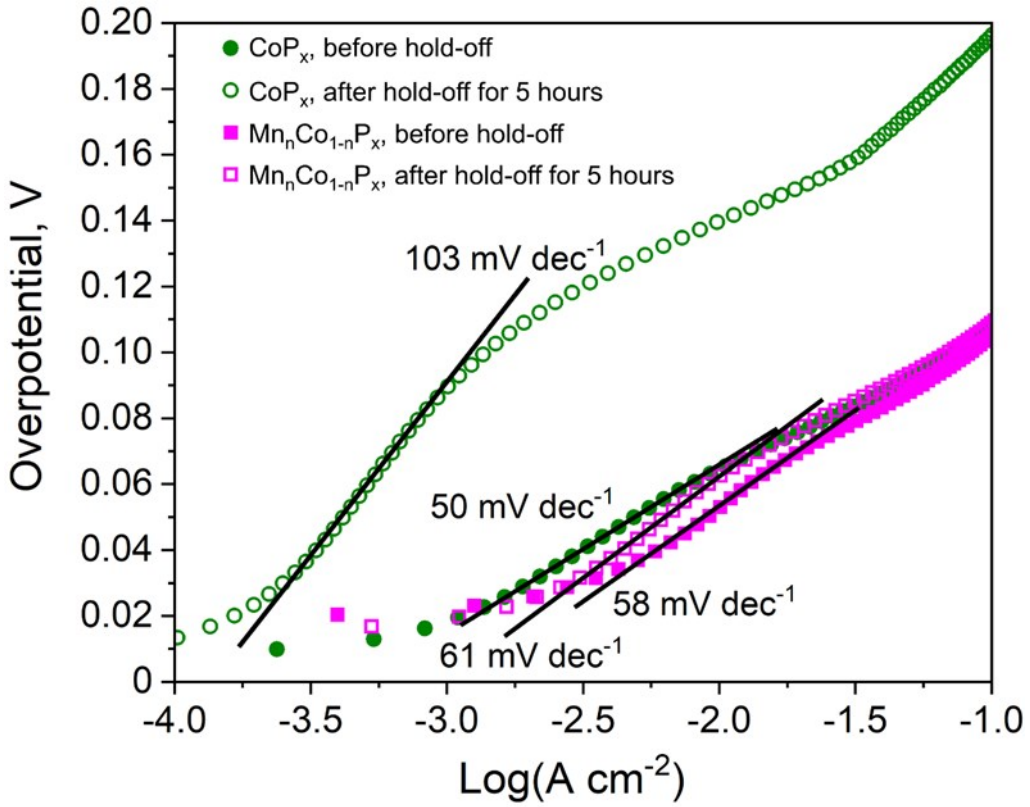

Fig. S15. Tafel plots for the CoP_x and $Mn_nCo_{1-n}P_x$ before and after hold-off conditions

Table S11. The compositions of electrodeposition baths for CoP_x and $Mn_nCo_{1-n}P_x$.

Chemicals	Composition (g/L)	
	CoP_x	$Mn_nCo_{1-n}P_x$
$CoCl_2 \cdot 6H_2O$	142.76	128.48
$MnCl_2$	-	11.87
$NaH_2PO_2 \cdot H_2O$	127.2	127.2
Glycine	45.04	45.04
Boric acid	6.18	6.18
Saccharine	0.5	0.5

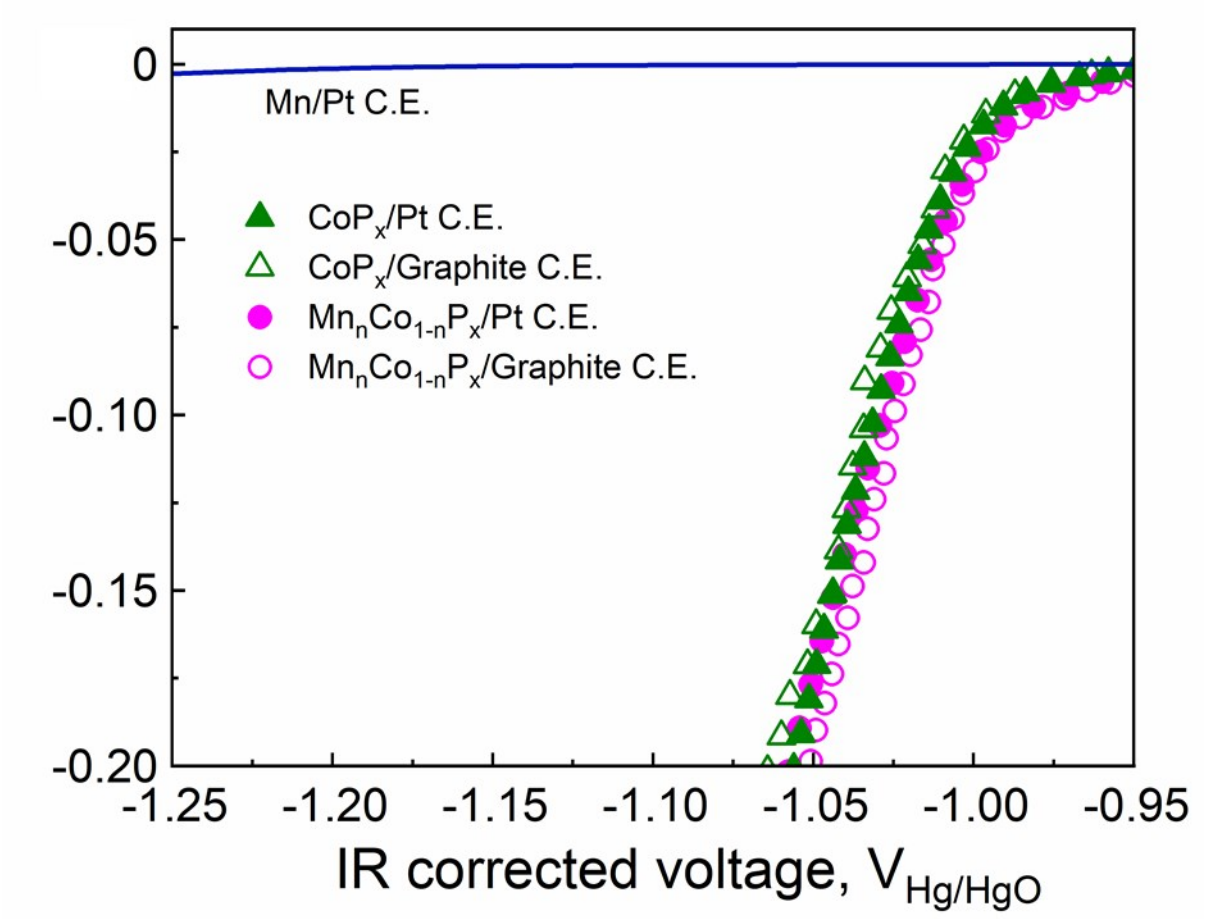

Fig. S16. LSV curves for HER on a CoP_x and $Mn_nCo_{1-n}P_x$ using a graphite carbon and a platinum plate as the counter electrode.

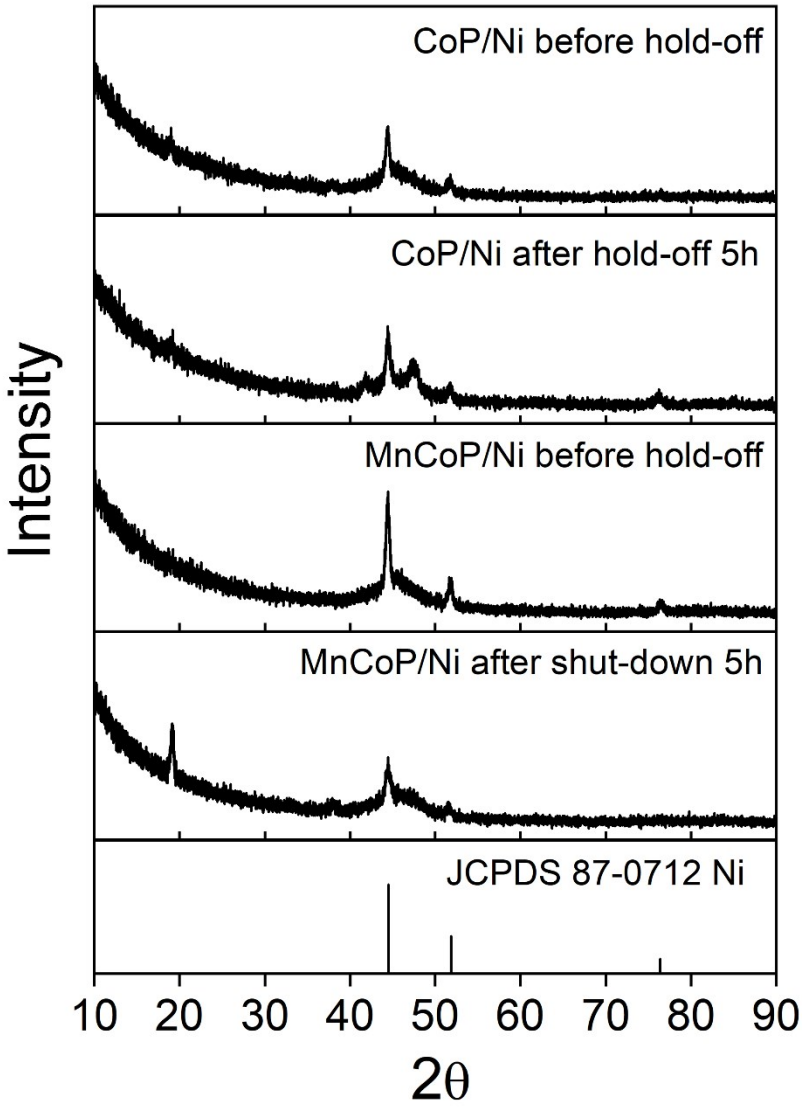

Fig. S17. XRD analysis for CoP_x and MnCoP on the Ni substrate.

References for Supporting Information

(1) Liu, T.; Ma, X.; Liu, D.; Hao, S.; Du, G.; Ma, Y.; Asiri, A. M.; Sun, X.; Chen, L. Mn doping of CoP nanosheets array: an efficient electrocatalyst for hydrogen evolution reaction with enhanced activity at all pH values. *ACS Energy Lett.* **2017,** *7* (1), 98-102. https://doi.org/10.1021/acscatal.6b02849

(2) Liu, T.; Liu, D.; Qu, F.; Wang, D.; Zhang, L.; Ge, R.; Hao, S.; Ma, Y.; Du, G.; Asiri, A. M. Enhanced electrocatalysis for energy-efficient hydrogen production over CoP catalyst with nonelectroactive Zn as a promoter. *Adv. Energy Mater.* **2017,** *7* (15), 1700020. https://doi.org/10.1002/aenm.201700020

(3) Tian, J.; Liu, Q.; Asiri, A. M.; Sun, X. Self-supported nanoporous cobalt phosphide nanowire arrays: an efficient 3D hydrogen-evolving cathode over the wide range of pH 0–14. *J. Am. Chem. Soc.* **2014,** *136* (21), 7587-7590. https://doi.org/10.1021/ja503372r

(4) Wang, J.; Yang, W.; Liu, J. CoP 2 nanoparticles on reduced graphene oxide sheets as a super-efficient bifunctional electrocatalyst for full water splitting. *J. Mater. Chem. A* **2016,** *4* (13), 4686-4690. https://doi.org/10.1039/C6TA00596A

(5) Zhu, Y. P.; Liu, Y. P.; Ren, T. Z.; Yuan, Z. Y. Self-supported cobalt phosphide mesoporous nanorod arrays: a flexible and bifunctional electrode for highly active electrocatalytic water reduction and oxidation. *Advanced Functional Materials* **2015,** *25* (47), 7337-7347. https://doi.org/10.1002/adfm.201503666

(6) Gu, S.; Du, H.; Asiri, A. M.; Sun, X.; Li, C. M. Three-dimensional interconnected network of nanoporous CoP nanowires as an efficient hydrogen evolution cathode. *Phys. Chem. Chem. Phys.* **2014,** *16* (32), 16909-16913. https://doi.org/10.1039/C4CP02613F

(7) Chang, J.; Liang, L.; Li, C.; Wang, M.; Ge, J.; Liu, C.; Xing, W. Ultrathin cobalt phosphide nanosheets as efficient bifunctional catalysts for a water electrolysis cell and the

origin for cell performance degradation. *Green Chemistry* **2016,** *18* (8), 2287-2295. https://doi.org/10.1039/C5GC02899J

(8) Wang, P.; Song, F.; Amal, R.; Ng, Y. H.; Hu, X. Efficient water splitting catalyzed by cobalt phosphide-based nanoneedle arrays supported on carbon cloth. *ChemSusChem* **2016,** *9* (5), 472-477. https://doi.org/10.1002/cssc.201501599

(9) Wu, T.; Pi, M.; Zhang, D.; Chen, S. 3D structured porous CoP 3 nanoneedle arrays as an efficient bifunctional electrocatalyst for the evolution reaction of hydrogen and oxygen. *J. Mater. Chem. A* **2016,** *4* (38), 14539-14544.

(10) Behl, W. K.; Toni, J. E. Anodic oxidation of cobalt in potassium hydroxide electrolytes. *J. Electroanal. Chem. Interf. Electrochem.* **1971,** *31* (1), 63-75. https://doi.org/10.1016/S0022-0728(71)80043-8

(11) Gong, L.; Liu, X. Facile synthesis and capacitive characteristics of Co (OH) 2 nanoflakes via a solid-reaction route at room temperature. *Materials Letters* **2011,** *65* (13), 2025-2028. https://doi.org/10.1016/j.matlet.2011.04.022

(12) Moon, S.; Vuong, N. M.; Lee, D.; Kim, D.; Lee, H.; Kim, D.; Hong, S.-K.; Yoon, S.-G. Co3O4–SWCNT composites for H2S gas sensor application. *Sensors and Actuators B: Chemical* **2016,** *222*, 166-172. https://doi.org/10.1016/j.snb.2015.08.072

(13) Liu, Y.-C.; Koza, J. A.; Switzer, J. A. Conversion of electrodeposited Co (OH) 2 to CoOOH and Co3O4, and comparison of their catalytic activity for the oxygen evolution reaction. *Electrochim. Acta* **2014,** *140*, 359-365. https://doi.org/10.1016/j.electacta.2014.04.036

(14) Du, J.; Li, C.; Wang, X.; Jones, T. G.; Liang, H.-P. Cobalt oxyhydroxide with highly porous structures as active and stable phase for efficient water oxidation. *Electrochim. Acta* **2019,** *303*, 231-238. https://doi.org/10.1016/j.electacta.2019.02.083